Ten Years of Speckle Interferometry at SOAR

Andrei Tokovinin
Cerro Tololo Inter-American Observatory, Casilla 603, La Serena, Chile; atokovinin@ctio.noao.edu

Abstract

Since 2007, close binary and multiple stars are observed by speckle interferometry at the 4.1 m Southern Astrophysical Research (SOAR) telescope. The HRCam instrument, observing strategy and planning, data processing and calibration methods, developed and improved during ten years, are presented here in a concise way. Thousands of binary stars were measured with diffraction-limited resolution (29 mas at 540 nm wavelength) and a high accuracy reaching 1 mas; 200 new pairs or subsystems were discovered. To date, HRCam has performed over 11,000 observations with a high efficiency (up to 300 stars per night). An overview of the main results delivered by this instrument is given.

Key words: instrumentation: high angular resolution – techniques: high angular resolution – (stars:) binaries: visual

Online material: color figures

1. Introduction

Speckle interferometry (SI) invented by Labeyrie (1970) is a well-known method of reaching diffraction-limited resolution at large telescopes, despite seeing and other distortions. It exploits the fine structure of short-exposure images caused by the interference of light. The same goal is achieved nowadays by means of adaptive optics (AO). However, AO works mostly in the infrared domain (hence with a lower resolution); it is more complex, while typical overheads make it less efficient than the SI or its flavor called "lucky imaging" (LI). However, both AO and SI/LI can work simultaneously, complementing and enhancing each other.

Early SI instruments built in the 1970s and 1980s employed electronic image intensifiers in conjunction with photographic film and, later, CCDs. Development of Electron-Multiplication (EM) CCDs capable of detecting single photoelectrons enabled a new, more performant generation of SI cameras. The High-Resolution Camera (HRCam) built in 2007 (Tokovinin & Cantarutti 2008) is one of the first such instruments. Other similar instruments are AstraLux (Hormuth et al. 2008; Hippler et al. 2009), the BTA speckle camera (Maksimov et al. 2009), DSSI (Horch et al. 2012), Robo-AO (Baranec et al. 2014), and AOLI (Velasco et al. 2016).

Current proliferation of SI/LI instruments is motivated by several science drivers. Discovery of exoplanets attracted attention to nearby stars and their resolved companions. On one hand, binaries perturb both photometry and radial velocities, forcing most exoplanet surveys to screen their targets with high spatial resolution. For example, follow-up of the *Kepler* objects is one of the main objectives of the speckle program at the Gemini telescopes. On the other hand, the need to understand the common origin of stellar and planetary systems has stimulated statistical surveys of stellar multiplicity, where the SI/LI became the enabling technology. Finally, the era of precise astrometry opened by *Hipparcos* and *Gaia* requires ground-based support to disentangle orbital motion of binaries in the astrometric reductions and to extend the limited temporal coverage of these missions. The science drivers call for observations of many hundreds or thousands of targets. The efficiency of SI largely surpasses that of typical AO instruments (note however Riddle et al. 2015) for a number of reasons (e.g., the need to acquire a guide star for AO), making it the method of choice.

The HRCam has been originally described by Tokovinin & Cantarutti (2008). The goal of this paper is to present this instrument and its subsequent upgrades in a more complete and systematic way. This includes the methods of data reduction, performance metrics, and the observing procedure, which evolved during ten years, reflecting the growing experience. To date, a large number of binary star measurements and discoveries resulted from observations made with HRCam, justifying detailed description of the instrument and its limitations in the present paper.

Section 2 describes the HRCam. Observations and data reduction are covered in Section 3, and some results from this instrument are presented in Section 4. The paper closes with a short summary in Section 5.

2. High-Resolution Camera (HRCAM)

2.1. Optics and Mechanics

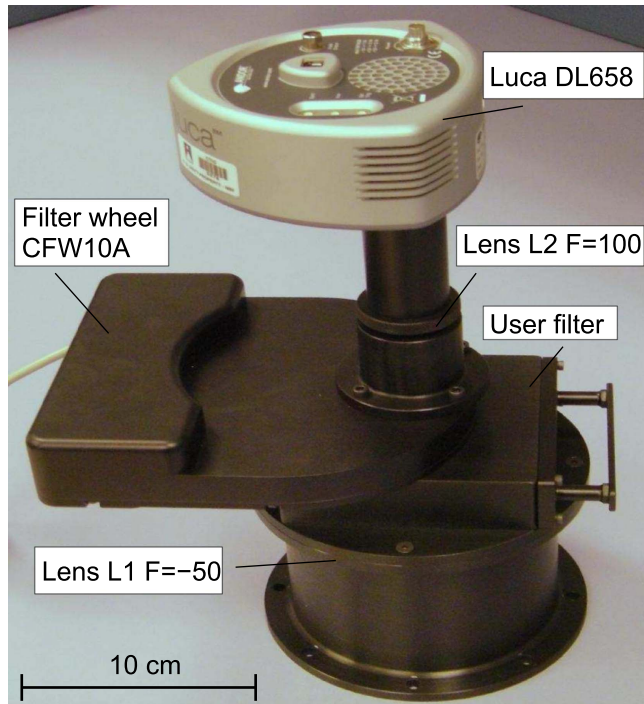HRCam works at the 4.1 m Southern Astrophysical Research (SOAR) telescope (Sebring et al. 2002). It was originally

Figure 1. HRCam and its main elements.
(A color version of this figure is available in the online journal.)

Table 1
Components of HRCam

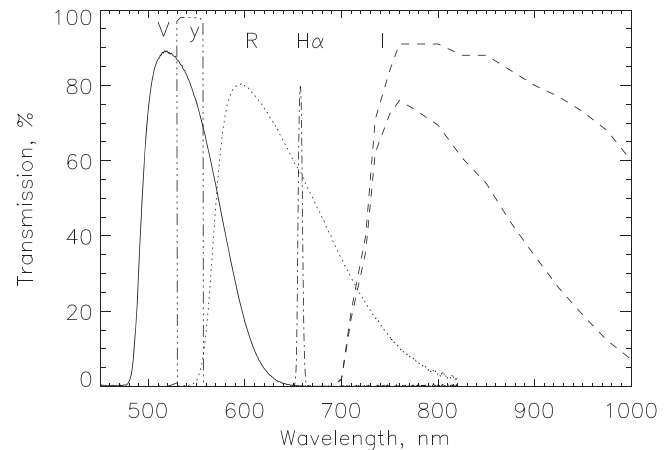| Element	Model	Vendor
Filter wheel	CFW10-SA	sbig.com
Filters, 1.25″ diam.	B, V, R, I, Hα	sbig.com
Filter y	543/22 nm, #76-032	edmundoptics.com
Negative lens	−50 mm, #62-492	edmundoptics.com
Positive lens	100 mm, #47-641	edmundoptics.com

Figure 2. Transmission curves of the HRCam filters. For the I filter, the lower curve is the product of the filter transmission and the QE of the iXon-888 CCD; the latter defines the cutoff at long wavelengths.

designed to help commission the SOAR Adaptive Module (SAM) in its initial configuration, where the natural guide stars were used (Tokovinin et al. 2016b). The choice of the EM CCD with 10 micron pixels called for the magnification of the F/16.5 SOAR focal plane by two times to ensure proper Nyquist sampling of speckles. This is done by the combination of two achromatic lenses, a negative L1 with $F = -50$ mm located in front of the focus and collimating the beam, and a positive lens L2 with $F = +100$ mm that refocuses the magnified image on the detector. This simple optics is diffraction-limited. Later HRCam worked with two other EM CCDs with smaller and larger pixels. In those cases, the L2 lens was replaced to approximately preserve the image scale of 15 mas per pixel.

Figure 1 shows the HRCam in its original configuration with the Luca EM CCD camera (see Section 2.2). Its commercial components are listed in Table 1. The mechanical design by P. Schurter is very simple and modular. The lower cylinder contains the negative lens L1. A box with a sliding frame is provided to hold a large user-defined filter; however, this option was used only for technical work with SAM. The commercial filter wheel is attached to the box and, in turn, holds the tube with L2, to which the camera is attached by its C-mount thread. The camera and L2 are mutually focused to infinity by adjusting the tube length. The tube is replaced when an L2 lens with a different focal length is installed.

Unfortunately, this mechanics allows axial rotation of the camera. Therefore, its position angle has to be adjusted at each re-installation.

HRCam has a set of standard B, VR, I filters of 1.25″ diameter in its filter wheel, as well as the narrow-band Hα filter with 5 nm bandwidth (Figure 2). The originally installed Strömgren y filter was cut out from the old interference filter with the central wavelength 551 nm, bandwidth 22 nm, and maximum transmission of 57%. It was later replaced by the commercial interference filter with a rectangular passband of 543/22 nm and an excellent transmission.

In 2017, the Luca camera was replaced by the more powerful detector, iXon-888 (see Section 2.2 and Table 2). This heavier camera required reinforcement of the mechanical structure, because it could no longer be held by the tube bolted to the thin wall of the filter wheel. A plate supported by the truss was designed to transfer the load of the camera directly to the mounting plate of HRCam. The camera is still connected to the tube, but is also firmly clamped to the new plate. The iXon-888 uses L2 with $F = 125$ mm to preserve the pixel scale.

HRCam is normally attached to the SAM as a user instrument. SAM relays the image without change of the plate scale, optionally correcting the seeing by its deformable mirror

Table 2
Characteristics of the Luca and iXon-888 EM CCDs

Parameter	Luca DL 658	iXon X3 888
Format H × V [pixels]	658 × 496	1024 × 1024
Pixel size [μm]	10	13
QE(540nm)	0.50	0.96
QE(790nm)	0.25	0.82
Response [el/ADU]	1.7	10.1
EM gain	1–300	1–1000
Readout noise [el]	15	45
CIC [el/pixel]	0.07	0.02

(DM). In most cases, the DM was passively flattened during speckle observations. However, for observations of faint targets, the AO compensation was used to concentrate the light, thus increasing the sensitivity. Another important function of SAM is to correct the atmospheric dispersion (AD); the AD corrector is described by Tighe et al. (2016). As SAM became available only in 2009, previous observations with HRCam were made without AD correction. In this case, the speckle elongation was accounted for in the data reduction.

The guide probe of SAM, located at the original (uncorrected) focus, can project a point source into the instrument. This capability is used to control the optical quality and to calibrate the focal plane of HRCam. The probe is moved laterally on its translation stages, and its images are recorded with HRCam. The position of the image centroids is approximated by the linear function of the coordinates, relating the detector pixels to the focal plane coordinates. Such relation is also determined for the regular SAM imager covering the 3′ field. Image orientation on the sky determined from the astrometric solution of the imager can thus calibrate the orientation of the HRCam detector.

2.2. EM CCD Detectors

Table 2 gives some characteristics of the Luca DL 658 (hereafter Luca) EM CCD used since 2007 and the iXon X3 888 (iXon-888) camera used in 2017. Both cameras are manufactured by Andor.[1]

The Luca uses the Texas Instruments line-transfer CCD. The charge is stored in light-protected areas near each pixel, to be transferred and amplified after the end of the exposure. The line-transfer architecture allows a very short exposure time without any image blur associated with the charge transfer. This feature turned out to be very useful at SOAR, allowing us to mitigate telescope vibrations by exposure times as short as 2 ms, if the star is sufficiently bright. As any front-illuminated CCD, the Luca detector has a modest quantum efficiency
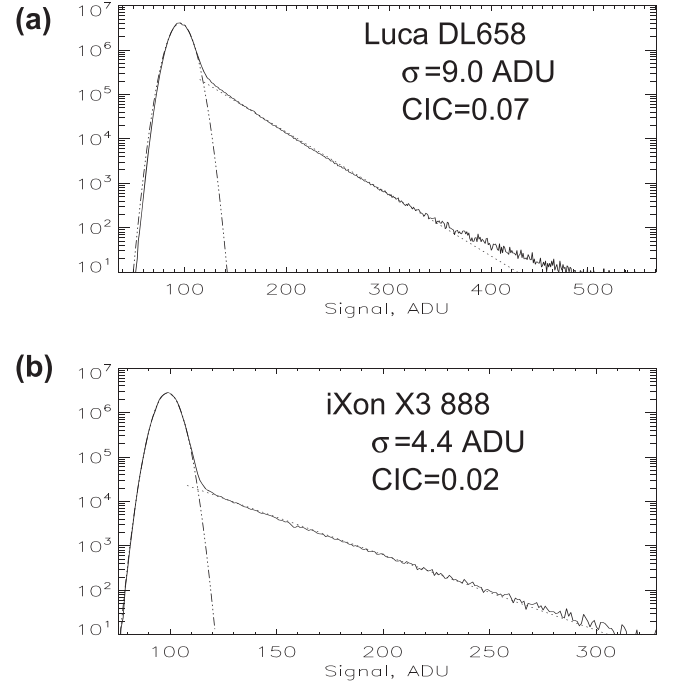
---
[1] www.andor.com

Figure 3. Histograms of signal in the bias images and their models: (a) Luca and (b) iXon-888. The histogram is plotted by the full line, the two terms of the model (1) by the dashed-dotted and dotted lines.

(QE) peaking at 0.5. The CCD is thermoelectrically cooled to −20 °C.

Dark images taken with the EM gain have a typical appearance: most pixels contain only noise, but some isolated pixels are bright. They correspond to the clock-induced-charge (CIC) generated and amplified in the EM register. Noise parameters of the EM CCD can be determined from the distribution of its signal (Figure 3). The signal histogram can be modeled by a sum of two terms: the Gaussian distribution corresponding to the readout noise and the decaying exponent that corresponds to the amplitude distribution of the CIC and photon events:

$$h(y) \approx h_{01} \exp\left[-\frac{(y - y_0)^2}{2\sigma^2} \right] + h_{02} \exp\left[-\frac{y - y_0}{a} \right]. \quad (1)$$

Here, σ is the readout noise, a is the typical amplitude of the amplified single-photon events, both in ADU. The CIC rate is the fraction of pixels with the signal level above 5σ from the bias value, y_0 (in this case, about 100 ADU). The Luca camera has a relatively high CIC rate of 0.07. Even the 200 × 200 image fragment thus contains about 3000 CIC events that dominate over the signal from faint stars and seriously limit the sensitivity of HRCam.

In 2014 July, the Luca camera failed: it simply lost any sensitivity to light. The camera was sent for repair to the

vendor and returned in working condition in early 2015. However, intermittent failures happened again in 2016 May, and the vendor suggested that the camera cannot be repaired anymore. In the observing runs of 2014 and 2016 December, we installed on HRCam the Luca-R cameras loaned from other programs. They also use front-illuminated EM CCDs from Texas Instruments, but with smaller 7.4 μm pixels (L2 of $F = 75$ mm was then installed) and with the frame-transfer architecture; the format is 1004×1002 pixels. We found that these cameras have a poor charge transfer efficiency (CTE) in the vertical direction, resulting in the loss of resolution. The blur depends on the signal level: it reaches 5–6 pixels for faint stars, but becomes negligible for bright ones. This signal-dependent blur had to be accounted for in the data processing, as described in (Tokovinin et al. 2015b). Obviously, the CTE problem degraded the resolution and the measurement precision. The CIC spikes in the Luca-R CCD are not blurred vertically by the poor CTE because they are not produced in the CCD pixels but rather generated during the readout.

In 2017, we started to use a much better iXon-888 camera, loaned to SOAR by N. Law (UNC). This EM CCD is back-illuminated and has a very good QE (Table 2). Moreover, its detector can be cooled to $-80\,°C$, resulting in the negligibly small dark current. The optics and mechanics of HRCam was adapted as described above. The new detector was characterized by a series of tests. Its EM gain actually corresponds to the gain setting (unlike Luca). All parameters match the specifications except the CIC rate, which was found to be around 0.06 el/pixel, significantly exceeding the 0.01 rate announced by the vendor. However, the CIC rate could be reduced to 0.02 by reducing the vertical transfer time to 3.3 μs, faster than the "minimum recommended" time of 6.5 μs. With this setting, the charge transfer was still perfect, but with an even faster clock the charge transfer stopped working and the CCD produced no images.

The iXon-888 camera contains a frame-transfer EM CCD, hence the minimum exposure time is restricted by the readout rate of 10 MHz per pixel. For the normally used region of interest (ROI) of 200×200 pixels (without binning), the minimum exposure time is 24.4 ms, and the fastest frame time is 27.9 ms. This exposure, used mostly in 2017, makes the results sensitive to the 50 Hz telescope vibration. With the 2×2 binning, the same ROI can have an exposure time of 13.5 ms (i.e., two times faster). An even faster operation is possible in the so-called cropped-sensor mode, where vertical stripes of selected width are shifted and read out continuously. In the cropped-sensor mode, the 200×200 ROI without binning can be exposed for 6.7 ms. However, in this mode the star must be located at 100 pixels from the left edge of the field, not at the center. The cropped-sensor operation was successfully tested on the sky, but not used routinely because

Table 3
Summary of Observing Runs

Dates	Camera	AO	Notes
2007.81—2007.82	Luca	No	First HRCam run
2008.53—2008.55	Luca	No	Blanco run
2008.60—2009.26	Luca	No	Without ADC
2009.66—2011.07	Luca	Yes	SAM in NGS mode
2011.28—2014.31	Luca	No	
2014.77—2014.86	Luca-R	No	Luca-R, poor CTE
2015.03—2015.92	Luca	No	Start using SAA
2016.04—2016.05	Luca	Yes	Young stars
2016.13—2016.14	Luca	No	
2016.38—2016.40	Luca	Yes	*Kepler* targets
2016.94—2016.97	Luca-R	No	Luca-R, poor CTE
2017.28—2017.83	iXon-888	No	New camera

switching between the modes cannot be done rapidly and thus affects the observing efficiency.

2.3. Computers and Software

The digitized video signal of the Luca camera is acquired through the USB interface. As the data-taking computer was located far from the instrument, we used the fiber optics signal extender. This configuration occasionally had connection problems. In 2015, we replaced the standard data-taking computer by the compact Intel NUC PC located at the telescope in the electronics rack, with direct USB connection to the camera. This has improved the reliability. However, this PC had no space for the PCI interface board of the iXon-888 camera that uses the Cameralink communication protocol. Moreover, the length of the Cameralink cable is only 2 m, forcing us to locate the newly purchased fan-less PC near the HRCam.

The HRCam software was developed by R. Cantarutti using the Software Development Kit (SDK) provided by Andor, as well as LabView. The software allows selection of the EM gain, exposure time, binning, and the ROI. Several settings of the ROI and binning (detector modes) are defined in the configuration file and normally used during observations. Once the detector parameters are set, the images are acquired continuously in the "run to abort" mode and displayed in real time, for centering and focusing. The desired number of sequential frames can be written as an image cube (16-bit integer numbers) into the FITS file. Its header contains information from the SOAR Telescope Control System (TCS) and from the SAM instrument, as well as the settings of the HRCam itself. The software has a convenient graphical user interface (GUI). Moreover, it provides for the display of the acquired cubes using the DS9 utility and an optional calculation and display of the power spectrum. This quick-look analysis capability is essential for evaluation of the data quality. When a new binary or triple system is discovered, this is usually immediately recognized, allowing the observer to take additional data for confirmation.

Table 3 gives the synopsis of the observing runs and the evolution of the instrument and observing technique with time. The column AO indicates the use of AO correction for some targets in the corresponding runs.

3. Observations and Data Processing

3.1. Observing Procedure and Tools

Accumulation of the standard cube of 400 frames takes only 11 s. The observing efficiency mostly depends on the time used to point the telescope and to set the instrument parameters. As has always been the case in speckle interferometry, careful preparation of the observing program and an efficient strategy are key ingredients for reaching high productivity. Previous speckle programs on 4 m telescopes could observe up to 200 stars per night; for example, 775 stars were measured in 4 nights at CTIO by McAlister et al. (1990).

The software for planning and executing HRCam observations is written in IDL. The observing program database contains essential information on all stars: names, equatorial coordinates, proper motions (PMs), magnitudes of the components, binary separation, and short comments indicating the reason for the observation and the priority. The date of the last measure is also stored and refreshed when new data become available. Tools exist for adding new objects to the program by retrieving information from the Washington Double Star Catalog (WDS) (Mason et al. 2001), from the *Hipparcos* catalog, or from a text file. Objects to be observed in the forthcoming run are selected from the general database. The program of each run always contains additional backup targets that can be observed under poor conditions.

Coordinates of selected objects are computed for the date of the observation, accounting for the PM, and formatted into a list, grouped by their position on the sky. Originally, the lists were loaded into the TCS, and the telescope operator was asked to point the telescope to the next target. Starting from 2014, this procedure has been automated using the new observing tool (OT). The OT displays part of the sky around the selected target in the horizontal coordinates, showing the adjacent targets. The size of the displayed region is selectable. The next target can be chosen by clicking in this display; its parameters (and, if needed, all previous measurements) are shown. By pressing the button in the OT GUI, the observer sends the coordinates to the TCS, while the name of the target is entered in the HRCam GUI. The telescope slews to the new target automatically if it is within 15° from its previous position; otherwise, the slew must be confirmed by the telescope operator. The OT substantially improves the productivity and, at the same time, reduces the stress of both the observer and the telescope operator, as well as the number of human errors.

The pointing of SOAR is good to ∼5″ rms. However, the field of view (FoV) of HRCam is quite small, only 15″ with the 1024^2 CCD. For target acquisition, the full camera field is used, with a small EM gain and an exposure time of 0.2 s. When the target is centered, the detector mode (ROI and binning), the exposure time, EM gain, and filter are selected. The zero-point command is sent to the TCS to refine the pointing, so that the next nearby star is often acquired in the same ROI without looking at the full field. A special command in the SAM control software sets the ADC according to the telescope coordinates and flattens the DM. The SAM can also command telescope offsets in position and focus. The focus is adjusted visually by observing the star in real time. A sequence of targets in the same area of the sky can be observed rapidly without any action of the telescope operator. In 2017 June, 306 stars were observed with HRCam in one night.

Normally, two data cubes, of 400 frames each, are recorded for each target and each filter. Given the small time needed for the acquisition of the extra cube, this practice does not affect the efficiency. Two (or more) cubes are processed independently and the final results are averaged, while their mutual agreement gives an estimate of the internal error. Acquisition of two data cubes guarantees from "glitches" such as an occasional cosmic ray in one of the frames and makes the detection of new companions more secure.

The standard detector mode is a 200 × 200 ROI (3″ × 3″ on the sky) without binning and 400 frames per data cube. Fainter stars are sometimes observed with a 2 × 2 binning and an increased exposure time. This increases the sensitivity at the expense of degraded resolution. Binary stars wider than 1″5 are observed with a wider 400 × 400 ROI (with or without binning) to avoid image truncation and aliasing. The wider ROI is also useful on the nights with a strong wind, when the telescope shake throws the star outside the 3″ field (we do not use guiding). The vast majority of observations are made in the *I* or *y* bands, while other filters are used only occasionally.

The image delivered by the telescope can be sharpened using the UV laser and the SAM AO system. As HRCam is mounted on SAM anyway, this option comes for "free". In this regime, we do not acquire guide stars with SAM, while the acquisition of the laser and closing the laser loop are fast (about a minute for large slews or a few seconds for small slews). However, the lists of the laser targets must be submitted in advance to the Laser Clearing House for approval of the laser propagation. Laser-assisted speckle runs were done for programs with faint targets (Schmitt et al. 2016; Briceño & Tokovinin 2017).

3.2. Data Cube Processing

The data cubes are processed by the custom IDL software to compute the power spectrum (PS) and auxiliary images. The PS is the square modulus of the Fourier Transform (FT) of the intensity distribution in each frame, averaged over all frames in the cube.

The optimum way to calculate the PS was found by experimenting with the real data. To reduce the impact of noise

in the "empty" pixels that do not contain star photons, the image is thresholded at ~20 ADU above the bias level. Signal histograms in Figure 3 show that such thresholding indeed cuts most of the readout noise.

Images taken with the Luca camera contain a number of "hot" pixels where the thermal signal is detectable even at short exposures. To account for this, two bias image cubes with different exposure time (e.g., 20 ms and 100 ms) are taken and median-averaged. From these data, the bias image corresponding to the zero exposure time and the dark current (in ADU/s) in each pixel are computed, for the full frame and the fixed EM gain used in the observations. Their combination with the actually used exposure time and ROI parameters is the bias level for each data frame, to be subtracted before the thresholding. If such correction is not done, hot pixels are clearly visible in the average images of faint stars. We do not apply flat-field corrections because the CCD sensitivity variations of a few per cent are much smaller than the speckle noise and their correction does not improve the quality of the final data products.

The dark current of the iXon-888 camera operated at $-60\,°C$ is negligible, so there is no need to account for hot pixels. On the other hand, the bias level in its images has a vertical (along columns) structure that does not depend on the EM gain but depends on the ROI and binning. To correct for this, bias image cubes are taken without EM gain for each ROI/binning combination. The median-averaged bias signal is subtracted from each column of the data frames.

The PS of speckle images of a point source, $P_0(\mathbf{f})$, has a characteristic two-component structure,

$$P_0(\mathbf{f}) \approx |T_{SE}(\mathbf{f})|^2 + 0.435(D/r_0)^{-2}T_0(\mathbf{f}), \qquad (2)$$

where $T_{SE}(\mathbf{f})$ is the seeing-limited short-exposure transfer function (FT of the average re-centered image), r_0 is the Fried parameter, D is the telescope diameter, and $T_0(\mathbf{f})$ is the transfer function of an ideal diffraction-limited telescope (see, e.g., Christou et al. 1985). The second term describes the high-frequency part of the PS, i.e., the speckles. In the image autocorrelation function, ACF (FT of the PS), the first term corresponds to the broad seeing-limited component, usually called "seeing pedestal", while the high-frequency term is responsible for the narrow diffraction-limited peak at the coordinate origin, the "speckle peak".

The PS of a binary or multiple star contains characteristic fringes. The ACF has corresponding secondary peaks at the separation ρ and position angle (PA) θ of the companion. However, the PS contains most energy at low spatial frequencies that produce the seeing pedestal in the ACF. The HRCam pipeline removes the seeing pedestal by computing the ACFs from the spatially filtered PS (Tokovinin et al. 2010a). The ACFs play an important role in the data processing. Wide binary companions are more readily detected in the ACF than

in the PS, while "fringes" produced by very close companions are more obvious in the PS.

The ACF is computed from the PS, i.e., the average square modulus of the image FT. This non-linear transformation extends the support of the ACF to twice the FoV size Ω. A correct ACF calculation, not implemented in the standard pipeline, should use the re-sampled PS. This matters only for wide binaries with separation $\rho \geqslant \Omega/2$. In such cases, the ACF computed by a simple FT of the (filtered) PS may have the companion's peaks in the wrong place due to aliasing. For this reason, wider FoV is used for observations of wide pairs; this also reduces the image truncation.

Apart from the PS, the pipeline computes the average image and the re-centered average image. A simple centroid algorithm works well in most cases. However, for faint stars, when the object flux becomes comparable to the CIC rate, the spurious events seriously bias the centroid. Centroiding of the smoothed and thresholded version of each frame works much better (see Schmitt et al. 2016). Centroiding also helps to reject frames where the star is too close to the edge of the field (e.g., because of the telescope wind shake).

Since 2015, the speckle pipeline also computes the shift-and-add (SAA) image centered on the brightest pixel in each frame. This is analogous to the "lucky imaging," except that no frames are rejected. A weight proportional to the signal in the brightest pixel is applied to each frame. These SAA images often contain the central diffraction-limited peak and the secondary peaks corresponding to the binary companion. Selection of the brightest peak resolves the 180° PA ambiguity inherent to the standard speckle processing. The SAA images are much noisier than the standard speckle ACFs because they do not use the information optimally (see the comparison between ACF and SAA in Tokovinin et al. 2010b). The SAA images of faint stars, centered on random photon spikes rather than on the real speckles, are useless, while binary companions are still detectable in the PS and ACF of these stars.

To summarize, the pipeline produces from each data cube four 2D images: PS, ACF, centered, and SAA (Figure 4). The headers of those images inherit information from the original image cube. This information also populates the database that holds results of the observations (see Section 4.1).

3.3. Fitting Binary and Triple Stars

Processing of HRCam data is described by Tokovinin et al. (2010a). Here, it is briefly recalled with an emphasis on the caveats. First, the photon-noise bias in the PS is determined by averaging it over the area beyond the cutoff spatial frequency $f_c = D/\lambda$ (λ is the wavelength, D is the telescope diameter). It is subtracted from the PS and accounted for while computing the noise.
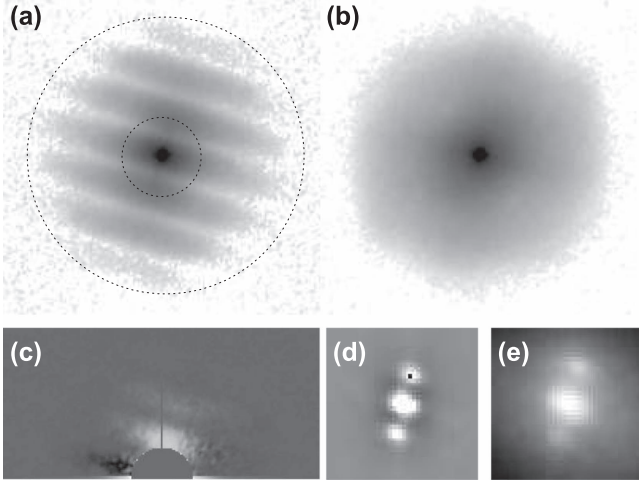
Figure 4. Example of data processing. The binary star WDS J01376−0924 (KUI 7) was observed in the y filter on 2017.83 with the iXon-888 camera. Binary parameters: $\rho = 0''.1229$, $\theta = 343°.4$, and $\Delta m = 1.22$ mag. Panel (a) shows the PS in negative logarithmic stretch, where the dotted circles mark the fitting zone between 0.2 and 0.8 f_c; (b) is the reference PS of the unresolved star; (c) is the residual to the model (upper half of the frequency plane in linear stretch); (d) is the central fragment of the ACF (the black point marks the companion's peak); and (e) is the fragment of the SAA image.

The PS of a multiple star with M components (point sources) is approximated by the model $P_{mod}(\mathbf{f})$

$$P_{mod}(\mathbf{f}) = P_0(\mathbf{f}) \, |\sum_{i=1}^{M} a_i \exp(2\pi \mathbf{f} \mathbf{x}_i)|^2, \qquad (3)$$

where $\mathbf{f}$ is the spatial frequency, $P_0(\mathbf{f})$ is the reference PS of a single star, a_i are the intensities of the components, and $\mathbf{x}_i$ is their coordinates. The PS is normalized to $P(0) = 1$, which translates to $\sum_i a_1 = 1$. Moreover, the PS is invariant to the translation of the source. Therefore, a multiple system with M components has $3(M-1)$ free parameters. Although the formula (3) looks simple, the square modulus contains cross-terms between all components, so the analytical expression of the derivatives of the model over parameters, needed for the model fitting, becomes complicated with increasing M. Model fitting is currently implemented only for binary and triple stars, delivering three and six parameters (PA, separation, and Δm), respectively, and their errors. For stars with four resolved components, additional positions and magnitude differences can be measured crudely from the peaks in the ACF.

For binaries with large angular separations $\rho \gg \lambda/D$, the PS contains multiple fringes. As a result, the binary's parameters are decoupled from the shape of the reference PS and the result of the fitting is very robust. In such cases, the rotationally averaged PS of the object itself makes a good reference $P_0(\mathbf{f})$ because the fringes are effectively removed by the averaging. For close binaries with separations on the order of λ/D, the analytic model of P_0 is used for fitting. This model, introduced in (Tokovinin et al. 2010a), is

$$P_{0,syn}(\mathbf{f}) = T_0(|\mathbf{f}|)\,10^{-[p_0 + p_1(|\mathbf{f}|/f_c)]}, \qquad (4)$$

where $T_0(f)$ is the transfer function of the ideal telescope. This model is valid only at high spatial frequencies $\lambda/r_0 \ll |\mathbf{f}| < f_c$. It is based on the theoretical expression for the speckle transfer function in the high-frequency domain (the second term of Equation (2)). The two parameters of the synthetic PS, p_0 and p_1, are determined by fitting the rotationally averaged PS. When the speckle structure is a perfect match to the theoretical model, $p_1 = 0$ and

$$(D/r_0)^2 = 0.435 \; 10^{-p_0}. \qquad (5)$$

In reality, the finite spectral bandwidth and the finite exposure time, as well as vibrations, reduce the speckle contrast at high spatial frequencies, leading to the faster PS decay, hence $p_1 > 0$. However, the parameter p_0 is still a valid measure of the average number of speckles, and the expression (5) holds, allowing us to compute r_0 and hence the seeing.

As the PS is symmetric, the binary or triple models are fitted only to the upper half of the frequency plane and in the restricted frequency range $0.2 f_c < |\mathbf{f}| < f_{max}$. By default, $f_{max} = 0.8 f_c$, but it is reduced for noisy data. Weights of individual pixels in the frequency plane are inversely proportional to the noise variance in these pixels, calculated analytically. The quality of the fit is determined by the usual χ^2/N parameter computed from the residuals and the noise. A perfect model results in $\chi^2/N \approx 1$. In practice, this happens for faint stars, while large χ^2/N are found for bright stars, where the residuals are dominated by un-modeled details of the PS.

Since 2015, we can use PS of other stars (both single and binary) as a reference (Tokovinin et al. 2016a). In the latter case, the fitted binary parameters serve to deconvolve the reference PS from the fringes, at the expense of the increased noise. Only binaries with fringes of low or moderate contrast ($\Delta m < 1$ mag) are suitable as reference. Naturally, the object and the reference must be observed in the same filter, with the same detector format, close in time and in the sky. Use of the real reference is particularly helpful in fitting difficult cases, such as binaries with small separation and a large Δm. As shown in Figure 4, even with the real reference, the residuals rarely resemble a white noise owing to systematic differences between the data and the model; in this particular case, $\chi^2/N = 13.3$.

In 2008 and 2009, when HRCam worked without AD correction, the PS model included speckle elongation caused by the AD. The elongation was computed from the known central wavelength and the bandwidth of each filter, knowing the telescope pointing. In 2014, the vertical blur caused by the poor CTE had to be included in the PS model (Tokovinin et al. 2015b).
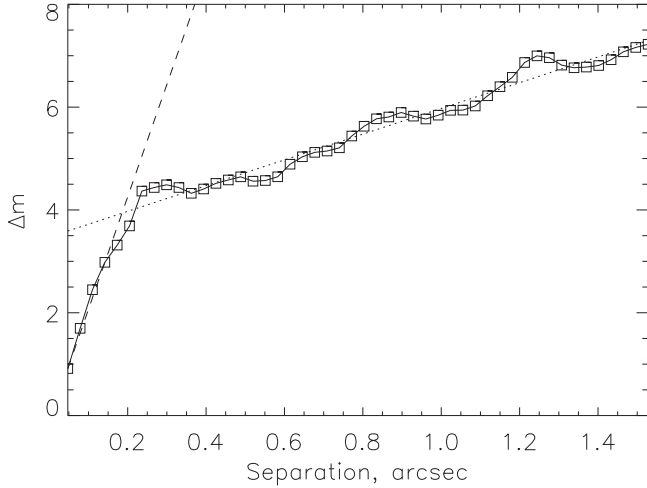
Figure 5. Detection limit for an unresolved star shown in Figure 4 (b); y filter, 200×200 ROI. The dashed and dotted lines are linear approximations at small and large separations, respectively.

3.4. Detection Limit, Resolution, and Sensitivity

The detection limits are estimated from the fluctuations of the ACF computed in annular zones of increasing radii. The rms amplitude σ is converted into the maximum detectable magnitude difference Δm by assuming that peaks larger than 5σ are detectable. This assumption has been verified on simulated companions (Tokovinin et al. 2010a). As shown in Figure 5, the detection limit $\Delta m(\rho)$ increases rapidly at small separations $\rho > 0\overset{''}{.}2$ and then continues to improve more gradually, reaching ~ 6 mag for good-quality data. The dynamic range of HRCam is comparable to other speckle instruments. Horch et al. (2012) can detect companions with $\Delta m \sim 5.5$ mag at $0\overset{''}{.}2$ separation (their Figure 5), on a larger telescope and with a larger number of accumulated frames. To give an example, the subsystem EHR 9 Ba,Bb (WDS J06454 -3148) is separated by $1\overset{''}{.}4$ from the main component A, and its components are ~ 6.5 mag fainter than A in the I band. It was measured with HRCam 10 times, leading to the calculation of the orbit with a period of 7 years (Tokovinin 2017). Note that at separations $\rho > 1''$ the speckle signal (and the detection limit) is reduced by the anisoplanatism; this seeing-dependent reduction is not accounted for in the computed curves like that in Figure 5. For binary stars, the curves $\Delta m(\rho)$ show sharp dips at the companion's separation.

The curves $\Delta m(\rho)$ at small and large separations are well approximated by two linear functions. The parameters of these linear fits are stored in `obsres` (see Section 4.1) and used to compute the detection limits at other separations. For unresolved stars, the published data tables give these limits at separations of $0\overset{''}{.}15$ and $1''$.

The nominal angular resolution of speckle interferometry equals the diffraction limit λ/D, i.e., 27 mas at 540 nm and

40 mas at 800 nm. At this separation, the maximum of the second fringe in the PS of a binary star coincides with the cutoff frequency f_c. However, when the data are of good quality (with the speckle signal at $0.8 f_c$ exceeding the noise), even closer binaries can be measured by fitting the PS model. Separations as small as 12 mas have been measured at 540 nm. On the other hand, for faint stars the PS is lost in the noise well before the f_c is reached, and the effective resolution is substantially worse than λ/D. The pipeline accounts for this by reducing the $f_{\max}$, and the resolution limits in the tables of unresolved stars are increased proportionally. However, the estimated resolution limits remain approximate and, possibly, optimistic.

The sensitivity (limiting magnitude) of speckle interferometry is a strong function of the seeing blur β (or, equivalently, of the Fried parameter $r_0 = 0.98\lambda/\beta$) because the number of speckles is proportional to $(D/r_0)^2$, i.e., to β^2. Faint stars are usually observed in the I band because of its larger bandwidth (hence larger flux) and the larger r_0. In practice, the magnitude limit reaches $I = 12$ mag under good seeing. Still fainter stars can be observed with a longer exposure time, at the expense of the spatial resolution. Considering that the seeing is variable and that the signal can be further degraded by vibrations, the magnitude limit cannot be guaranteed in the forthcoming observing runs. Under very poor conditions (poor seeing and/ or transparent clouds), good-quality measurements of bright stars are still possible.

The new iXon-888 camera exceeds the sensitivity of Luca in the I band by at least a factor of two, owing to its larger QE. Additional gain is provided by its lower CIC (Table 2). This camera is used since 2017 April. During this period, only one half-night of good seeing was experienced. On that night, a binary star with $I = 14$ mag was resolved, demonstrating the increased sensitivity of iXon-888.

The image size β can be improved by the SAM AO system. This observing mode was used twice for programs with predominantly faint targets (Schmitt et al. 2016; Briceño & Tokovinin 2017). With a longer exposure time and the 2×2 binning, not much is left of the speckle signal. However, the re-centered images are still quite sharp and allow discovery and measurement of binaries down to $\sim 0\overset{''}{.}1$.

3.5. Artifacts

It is well known that small vibrations of the telescope optical axis, irrelevant for seeing-limited observations, can be very detrimental to speckle interferometry. Unfortunately, the SOAR telescope is often affected by vibrations with a frequency of 50 Hz and an amplitude reaching 30 mas. They are present in the signals of the guiders and in the AO data recorded by SAM. The optical axis oscillates on an elliptical trajectory with variable eccentricity, from nearly circular to nearly linear. The amplitude of these oscillation is variable in
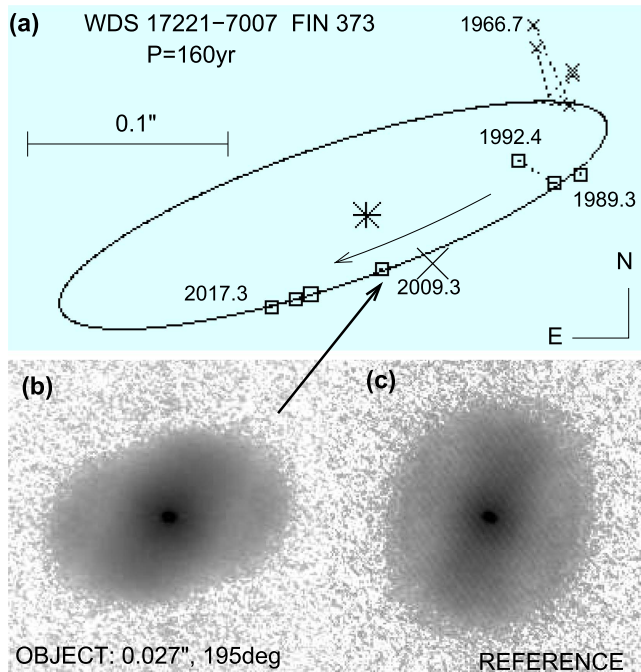
Figure 6. Orbit of the close binary WDS J17221−7007 (FIN 373) is shown in (a). Squares denote speckle measurements, crosses are the historic visual measurements by W. Finsen. The published measurement made with HRCam in 2009.3 (large cross) is wrong because the "fringe" in the PS (b) caused by vibration was originally interpreted as the binary-star signature. Use of the real reference (c) produces the correct measurement with $\rho = 27$ mas and $\theta = 195°$.

(A color version of this figure is available in the online journal.)

Figure 7. Optical ghosts and their simulation. The ACF of the $0\rlap{.}''12$ binary with OGs observed on 2008 August in the Hα band is shown in (a); each peak is surrounded by two spurious maxima. The OGs are simulated in (b) by combining seeing with the sine phase wavefront distortion of 0.4 μm amplitude and 2 m period. The OGs with two maxima recorded in 2016 February at 540 nm are shown in (c) for a single star. The simulated ACF in (d) is produced by a combination of seeing with the clipped sine wave of 0.2 μm amplitude and 1 m period.

time and depends on the telescope pointing (larger at low elevations). See Section 3 of (Tokovinin et al. 2010b) for more information on these vibrations. Our current understanding is that they are excited by vibrations of the soil with the 50 Hz frequency produced by electrical equipment such as transformers. The 50 Hz signal is indeed detected by the accelerometers installed at the telescope pier and at the top end of the telescope itself. However, the amplitude of these mechanical vibrations is an order of magnitude too small to explain the oscillations of the optical axis, and their waveform is not elliptical. Plausibly, the servo-controlled fast tip-tilt mirror of SOAR amplifies the 50 Hz mechanical perturbation under some, still unidentified, conditions.

The elliptical blur of speckles caused by the vibrations leaves a characteristic signature in the PS; for quasi-linear motion, the PS acquires a fringe-like structure and can mimic a binary star. One such difficult case is illustrated in Figure 6. Fortunately, another star with a similar vibration distortion can be used as a reference and allows to measure the parameters of close pairs, which often happen to be critical for the orbit calculation.

The vibrations reduce the high-frequency power and hence the sensitivity and/or resolution. Bright stars were normally
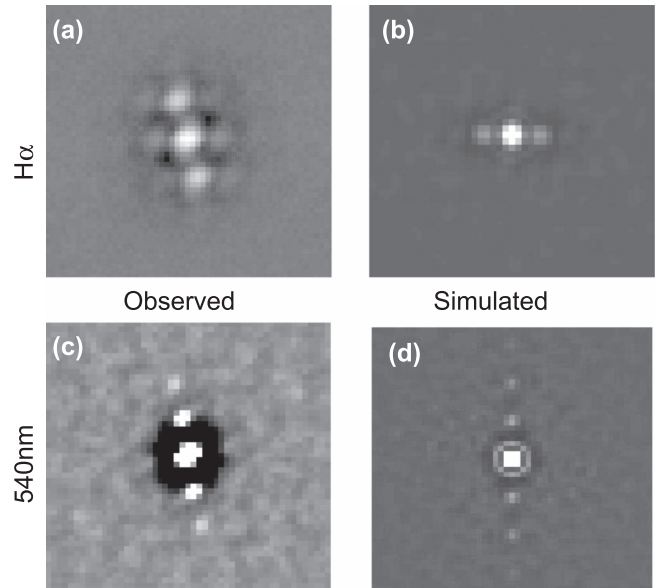
observed with the exposure time of 5 ms or shorter, possible with the Luca camera. This strategy recovers the resolution at the expense of the sensitivity. With the new iXon-888 camera, the typical exposure time is 24 ms, so we can only count on the intermittent nature of the vibrations. Sometimes they vanish completely and the PS extends almost to the cutoff frequency, as in Figure 4. Observations of the same star with a different exposure time is a good diagnostic of the vibrations.

Yet another phenomenon that can mimic a binary star is encountered sometimes under conditions of slow wind. Each peak in the ACF is then surrounded by two spurious faint peaks, often located at $\sim2\lambda/D$ separation, near the first diffraction ring. Unlike real binary companions, the separation of these optical ghosts (OGs) is proportional to the wavelength, hinting on their diffraction nature. Indeed, the OGs can be reproduced in simulation if random atmospheric wavefronts caused by the seeing are combined with a fixed periodic phase screen. Examples of the real and simulated OGs in the top row of Figure 7 are taken from the data obtained in 2008 (Tokovinin et al. 2010a). In 2016 February, the OGs with double diffraction spikes were seen, appearing and disappearing intermittently during a period of an hour (Tokovinin et al. 2018). Those OGs correspond to the phase perturbations with a spatial period of ~1 m and a non-sinusoidal shape. The OGs are most likely produced in the air near the telescope

when the wind speed is slow. Their dependence on the wavelength and similar appearance in different stars helps to distinguish OGs from real binary companions. Otherwise, the OGs can be mistaken for binary companions with $\Delta m \sim 3$ mag and separations from 60 to 120 mas.

Apart from vibrations and OGs, the shape of the PS is affected by the residual optical aberrations, especially under good seeing and/or at longer wavelengths. The observed PS always has some structure that lacks axial symmetry. This structure depends on many variable factors, such as the telescope focus. Two objects observed in a short succession in the same filter often have similar PS structure. Using one of the stars as a reference for another helps to account for the PS asymmetry and reduces its influence on the measurement accuracy. Such structure is notable in the PSs shown in Figures 4(a) and (b).

4. Results

Presently (2017 November), the total number of observations made with HRCam is 11903 (Table 3). This includes the 6-night run at the Blanco telescope in 2008, when HRCam was used as a substitute for the USNO speckle camera; all other observations were made at SOAR. The total number of observed objects is 4366; 2819 of those are resolved pairs, for which 8985 measurements were made. The WDS contains approximately 250 close binaries or subsystems discovered with HRCam. A total of 25 refereed publications use the HRCam data.[2]

4.1. Data Management

Reduction of the data cubes is just the first step in the speckle pipeline. Managing a large number of observations requires special tools to do this efficiently. Figure 8 illustrates the data flow in the speckle pipeline, from raw image cubes to the final tables of calibrated measurements. This process is explained below. As the pipeline is implemented in IDL, the results are stored and manipulated as IDL structures, depicted by the colored ovals in the Figure. The alternative, more traditional ways of using FITS headers, text files, or spreadsheets to store the processing results are less convenient.

Relevant information from the FITS headers is stored in the `log` structure, one element per data cube. It also holds the intermediate results (e.g., the parameters p_0 and p_1 and the total flux from the object). The `log` is compared with the observing program to identify wrongly typed object names and to add a tag corresponding to the particular program. It is checked for missing TCS information such as date and coordinates. In the rare cases of such errors, the missing information can usually be copied from the second data cube of the same object.
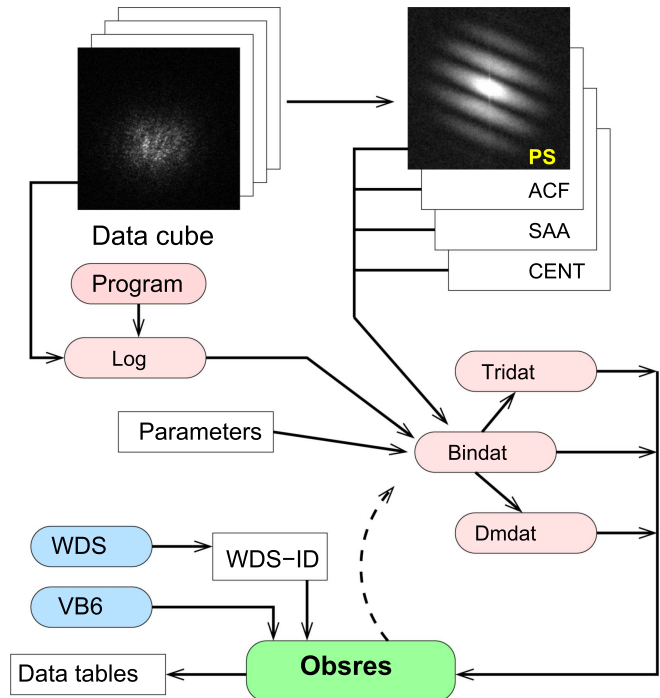
---

[2] See the bibliography at http://www.ctio.noao.edu/~atokovin/speckle/.

Figure 8. Data flow in the speckle pipeline. Colored ovals are IDL structures, unfilled rectangles are text files.

(A color version of this figure is available in the online journal.)

The *parameter file* plays a key role in the processing of each observing run. It specifies the directories where the images are stored, the calibration parameters (translation from the pixel coordinates to the sky coordinates), and the files that hold the data structures. Each observing run has its unique parameter file.

The `bindat` structure, produced from the `log`, is used to organize the binary-star processing. An IDL GUI serves to display the ACF, identify the binary companion by clicking on it, and to fit the binary parameters. It allows to display other associated images (PS, SAA, or centered) by a simple click and to navigate between all data of the observing run. Unresolved stars are marked by setting the total number of components M to one, triple stars have $M = 3$. The `bindat` also stores information on the detection limits. Although the binary-star fitting is interactive, it can be done rapidly and efficiently using the IDL GUI.

Stars marked as triple are processed by another GUI program which saves the results in the associated structure `tridat`. Alternative photometry of classically resolved binaries that uses centered images is done automatically, based on the information provided in `bindat`; its results are stored in the `dmdat` structure.

The correspondence between data cubes and measures is not straightforward. On one hand, two or more data cubes of the same binary star are averaged and produce only one

measurement. On the other hand, observation of a triple star produces two measurements of its subsystems that must be stored with different names. Published measurements of binary stars should be provided with their identifiers in the WDS catalog (Mason et al. 2001) and the standard names ("discovery codes"), if those exist. So, the results of the processing contained in `bindat`, `tridat`, and `dmdat` are combined, averaged, and stored in the final data structure, `obsres`, where one element corresponds to one observation of a particular subsystem in one filter.

After the averaging, each observation has its internal WDS code, generated from the coordinates, and the object name inherited from `bindat`. Triple stars have additional internal tags to distinguish between their two subsystems. The WDS catalog, previously transformed into an IDL structure, is searched by coordinates to find entries corresponding to the observed pair. If the WDS contains several binaries with the same code, the one with the best-matching separation is selected, while the rest are listed as alternative suggestions. The result of this automatic identification is the `WDS-ID` text file that translates internal object names into the official WDS names. For objects not found in the WDS, the internal names are kept. This "dictionary" needs only minor manual edits because the automatic match succeeds in most cases. The dictionary is used in creating the `obsres` structure, where the objects have their official names and WDS codes. The file name of the first averaged data cube is kept in the `obsres` as well, associating each measure with the images. The text files of the data tables are generated (exported) from the `obsres` structure.

The `obsres` structure is the final product of the speckle pipeline. Its elements are identified with the *Hipparcos* catalog to create alternative object names. The Sixth Catalog of Visual Binary Star Orbits, VB6 (Hartkopf et al. 2001), is searched for orbits of the observed binaries to compute the ephemeris positions and to compare them with the measures. There is a GUI program for browsing and editing `obsres`. It allows to look back at the corresponding images. This is done by associating the date of the observation with the parameter file of the corresponding observing run; then the binary-star GUI is called with these parameters and the file name of the data cube. This capability helps to examine questionable measures and to re-process them, if necessary, thus updating the `obsres`.

The last step in the speckle data reduction is the manual check for errors and inconsistencies that almost always happen in large data sets. For example, if, after pointing the telescope to a new target, the observer forgot to change the object name, the observations of two binaries will be averaged together, producing a wrong measure with a large internal error. This situation can be corrected during creation of the `log` structure, during the binary-star processing, and, finally, by accessing and re-processing the data from the `obsres` GUI. If several orbits for a given binary are found in the VB6, the choice can be made manually. If the star is not found in *Hipparcos*, its alternative name is entered manually, too.

The results of all observing runs can be joined (glued) together in the common `obsres` structure. It can be consulted by the OT during the observations, used to extract measures for orbit calculation, or to compare the latest observations with the previous ones. As mentioned above, at present it contains 11903 entries.

4.2. Calibration

Owing to the small FoV of speckle cameras, calibration of their pixel scale and orientation has always been difficult. For the HRCam, the following methods were tried:

- Calibration against visual orbits. The accuracy of most orbits in the VB6 catalog is inferior to the accuracy of the HRCam measurements, so this method, used only for the very first observing run, is questionable. It is still adopted by some speckle programs, however.
- Calibration using interference fringes is a standard technique, in use since the 1980s. In the case of HRCam, installation of a double-slit mask in the telescope beam is not practical. In 2009, the instrument was calibrated by a two-beam laser interferometer with a 0.5 m baseline attached to the telescope spider (Tokovinin et al. 2010b).
- Astrometric calibration of the SAM imager and its translation to the HRCam was used several times (see Section 2.1).
- Internal calibration using several wide binaries with a well-modeled slow motion is the preferred method described below. It was introduced in 2014 (Tokovinin et al. 2015b) and has been used since then. It can be applied retroactively to all HRCam measurements.

In 2017, the initial set of calibrators was extended to 65 pairs with separations from $0\rlap{.}{''}5$ to $3''$, each observed at SOAR at least three times (on average 8.6 times per binary). Their motion was modeled either by linear functions of time or by orbits, specially adjusted to fit the SOAR data. One such pair, HDS 333, is featured in Figure 9. For each run, the average correction in angle $\Delta\theta = \langle \theta_{\mathrm{obs}} - \theta_{\mathrm{model}} \rangle$ and the average scale factor $s = \langle \rho_{\mathrm{obs}}/\rho_{\mathrm{model}} \rangle$ are determined. After applying these corrections, the models of the binary motion are refined. After two iterations the process has converged. The rms deviations of the corrected measures from the models range from 1 to 3 mas in most cases.

Figure 10 shows the calibration parameters of all 51 observing runs and their rms scatter. Typical speckle runs have the rms scatter of the calibrators from $0\rlap{.}°1$ to $0\rlap{.}°2$ in PA and from 0.002 to 0.004 in scale. The runs of 2016 May and 2016 December have a larger than usual PA scatter of $0\rlap{.}°5$ and $0\rlap{.}°3$, respectively. The most deviant point in the upper plot of Figure 9 is that of 2016.96, contributing to the larger rms in the
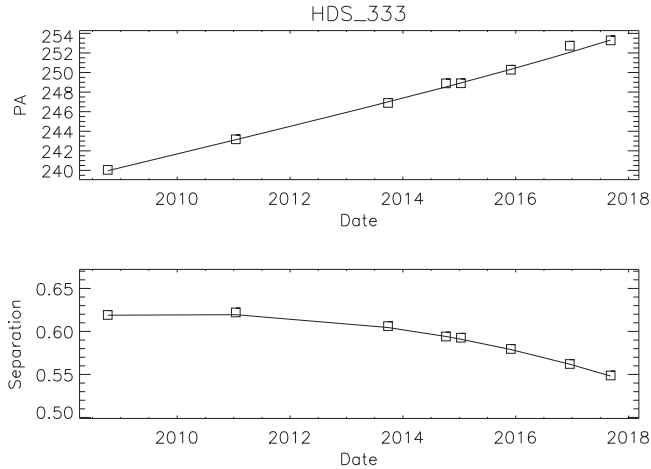
Figure 9. Observations of the calibrator binary WDS J02332−5156 (HDS 333) in PA (top) and separation (bottom) are plotted as squares, their models as full lines. Eight measurements have the rms residuals of 2.8 mas in tangential direction and 0.9 mas in separation.
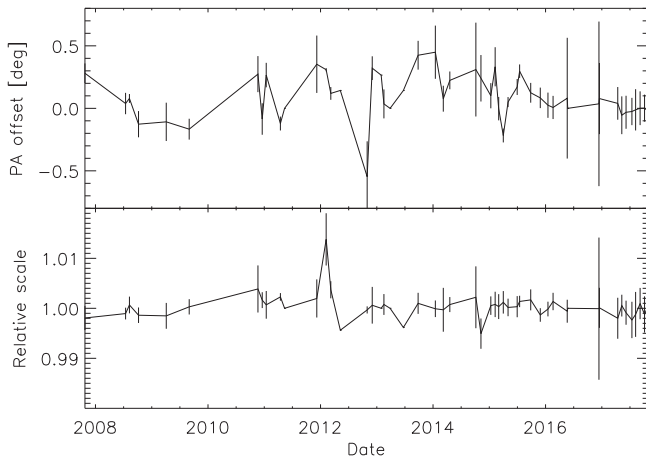

Figure 10. Offsets in PA $\Delta\theta$ and average scale factors s for the 51 observing runs made with HRCam since 2007, as determined from the calibrator binaries. Vertical bars show the rms scatter of calibrators in each run.

tangential direction. Apparently, the control of the Nasmyth rotator of the SOAR telescope had some problems in those two runs, degrading the accuracy of the PA setting.

It is desirable to observe the same calibrators with other speckle instruments in order to link their results with those of HRCam. Future more accurate measurements (e.g., with long-baseline interferometers or from space) may improve the calibration of already published data by using common binaries with well-studied motion.

4.3. Orbit Calculation

The large set of measurements of close visual binary stars obtained with HRCam is used for calculation of their orbits and

for improvement of already known orbits. The VB6 catalog currently contains more than 400 orbits based on the HRCam data, amounting to 15% of all entries. These orbits are published in (Gomez et al. 2016; Hartkopf et al. 2012; Mendez et al. 2017; Mason et al. 2010; Tokovinin 2012; Tokovinin et al. 2014, 2015a, 2015b; Tokovinin 2016a, 2016b, 2016c, 2016d; Tokovinin & Latham 2017; Tokovinin 2017). Figure 6 illustrates the orbit of the close binary FIN 373 based on four HRCam measures and two previous speckle measures. The prior orbit of this pair published in 2013 misinterpreted even the sense of the orbital motion (in fact it is retrograde, i.e., clockwise). Tokovinin (2016c) corrected this aspect, but computed an orbital period $P = 56.9$ yr, while the longer period $P = 160$ yr fits the data better.

In the least-squares fitting of the orbital elements, the weights should be inversely proportional to the square of the measurement errors. Good visual micrometer measures have an accuracy reaching 20 mas. The HRCam data have typical errors of 2 mas, calling for the relative weight of 100. Many visual measurements have much larger errors, e.g., $0\rlap{.}''2$, and their weights should be reduced accordingly to 10^{-4}. The system of weights adopted by the USNO team (Hartkopf et al. 2001) is much more uniform. As a result, old inaccurate data "drag" the orbit away from the best solution, and its residuals to the modern measures are larger than their errors. This is the case for many orbits published in (Tokovinin et al. 2015b).

To illustrate the potential of accurate HRCam measurements, the orbit of the subsystem TOK 44 Aa,Ab in the quadruple system HD 91962 (Tokovinin et al. 2015a) is displayed in Figure 11. This subsystem was first resolved at SOAR in 2009 and now the measures cover almost one full orbital period of 8.8 years. All measurements but one are from HRCam. The orbit is a combined solution that uses radial velocities (RVs) and includes the motion in the inner (unresolved) subsystem Aa1,Aa2 with the period of 0.47 year and the estimated semimajor axis of 18.4 mas. The mass of the component Aa2 is 0.3 $\mathcal{M}_\odot$, much smaller than the mass of Aa1, 1.14 $\mathcal{M}_\odot$, preventing the direct resolution of the inner pair at SOAR. However, its motion produces a detectable "wobble" in the relative position of Aa,Ab. The wobble was included in the orbital model by fitting the orientation, inclination, and astrometric axis α of the inner orbit together with the positional measurements of Aa,Ab and the RVs of Aa. The derived elements of the inner pair Aa1,Aa2 are $\alpha = 4.2 \pm 0.8$ mas, $\Omega = 21° \pm 11°$, and $i = 73° \pm 12°$. The amplitude of the wobble, α, matches its estimate given in (Tokovinin et al. 2015a). The relative inclination between two orbits computed from the new elements is small, $\Phi = 32° \pm 12°$, justifying the assumption of orbit coplanarity made in that paper. The rms residuals of Aa,Ab in two coordinates are 2.2 and 2.1 mas. If the wobble amplitude is set to zero, the residuals increase to 2.9 and 2.7 mas. This object is a triple star (the outer pair A,B is resolved at $0\rlap{.}''93$). Despite this
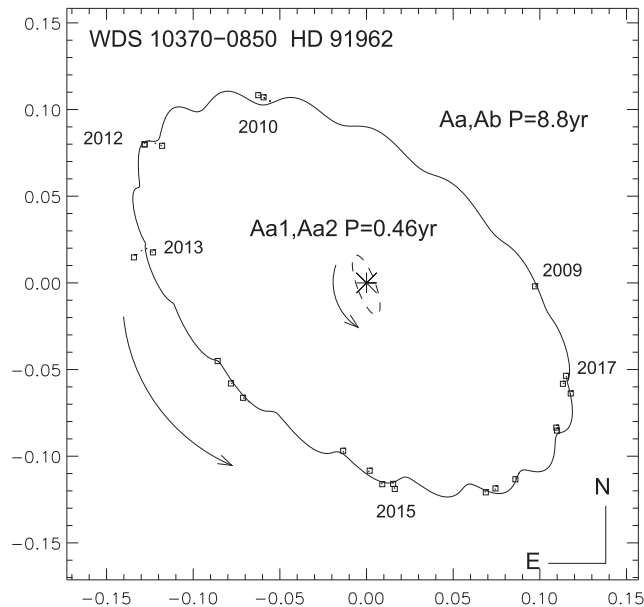
Figure 11. Observed motion of the subsystem TOK 44 Aa,Ab in the quadruple star HD 91962 is modeled by two sets of orbital elements with periods of 8.8 and 0.47 years (full line). The measurements are plotted as squares and connected to the ephemeris positions by the short dotted lines. The orbit of the inner (unresolved) subsystem Aa1,Aa2 is shown by the dashed line; it causes the "wobble" in the observed motion of Aa,Ab. The scale is in arcseconds.

complication, the measurements of the inner subsystem are very accurate. Modeling of the wobble in another triple system, HIP 103987, leaves the rms residuals of only 1.5 and 1.8 mas (Tokovinin & Latham 2017).

4.4. Surveys

The large number of objects that can be observed with HRCam in one night favor its use for multiplicity surveys. The first discoveries of 48 close binaries and subsystems were unexpected (Tokovinin et al. 2010a). Later, known visual binaries in the solar neighborhood were observed systematically to constrain the frequency of inner subsystems (Tokovinin 2014b). This effort has helped to improve the multiplicity statistics (Tokovinin 2014a). Some of those subsystems now have computed orbits (e.g., Figure 11).

The HRCam was used to survey 75 *Kepler* objects for multiplicity (Schmitt et al. 2016), although the bulk of such work has been done so far by other teams. As most of those stars are fainter than $I = 12$ mag, the sensitivity was improved by closing the AO loop. The same strategy was used in the multiplicity survey of young stars in the Ori OB1 association, conducted in 2016 (Petr-Gotzens et al., in preparation). As part of the same program, 10 new young binaries in the ϵ Cha association were discovered by Briceño & Tokovinin (2017). It

is noteworthy that 47 stars of this program were observed in 3.2 hours of telescope time.

5. Summary and Outlook

Systematic use of the new speckle camera at the SOAR telescope has started in 2008 and continues at present. Thousands of accurate measurements of binary stars delivered by this instrument have allowed substantial improvement of hundreds of visual orbits and calculation of many new orbits. The impact of this data set will extend far into the future. More than 200 close binaries or subsystems were discovered with HRCam, contributing to the improved statistics of binary and multiple stars.

HRCam was recently equipped with the new, more performant detector, with a better magnitude limit which can be further boosted by using the SAM laser AO system. The high efficiency of HRCam at SOAR (hundreds of stars per night) makes it an instrument of choice for large surveys, surpassing the capabilities of the existing AO systems on large telescopes. It will be an ideal instrument for the follow-up of the TESS targets, all brighter than $I \approx 12$ mag. With the current efficiency, the expected 3000 exoplanet host candidates to be discovered by TESS can be observed in 10 nights. In a survey mode, the productivity of HRCam observations can be further improved by using fixed instrument configuration and automating the star centering and data taking.

Many HRCam targets are relatively bright, with enough photons to correct the wavefront in real time. This operational mode has been demonstrated in 2009–2010 during commissioning of SAM (Tokovinin et al. 2010b), but this capability is lost now because SAM is permanently configured for the UV laser. If a small dedicated AO system with a narrow FoV were built, it would greatly benefit the speckle program. It could use one region of the spectrum (e.g., green) for wavefront sensing while the remaining wavelengths would go to the HRCam detector. The concept of such instrument has been proposed by Law et al. (2016). It will be installed at the presently unused side port of SOAR, without image rotation. For faint targets, the AO compensation will be partial, but still useful, correcting in real time focus and low-order aberrations to get the smallest possible β. Brighter stars will be fully compensated, allowing long exposures for such challenging programs as high-contrast imaging and/or resolved spectroscopy. A similar combination of AO and SI/LI is implemented in the AOLI instrument (Velasco et al. 2016).

and R. Mendez helped the author to improve it. The detailed comments provided by the anonymous referee were also helpful.

References

Baranec, C., Riddle, R., Law, N. M., et al. 2014, ApJ, 790, 8
Briceño, C., & Tokovinin, A. 2017, AJ, 154, 195
Christou, J. C., Cheng, A. Y. S., Hege, E. K., & Roddier, C. 1985, AJ, 90, 2644
Gomez, J., Docobo, J. A., Campo, P. P., & Mendez, R. A. 2016, AJ, 152, 216
Hartkopf, W. I., Mason, B. D., & Worley, C. E. 2001, AJ, 122, 3472 (VB6)
Hartkopf, W. I., Tokovinin, A., & Mason, B. D. 2012, AJ, 143, 42
Hippler, S., Bergfors, C., Brandner, W., et al. 2009, Messenger, 137, 14
Horch, E. P., Howell, S. B., Everett, M. E., & Ciardi, D. R. 2012, AJ, 144, 165
Hormuth, F., Hippler, S., Brandner, W., et al. 2008, Proc. SPIE, 7014, 48
Labeyrie, A. 1970, A&A, 6, 85
Law, N. M., Ziegler, C., & Tokovinin, A. 2016, Proc. SPIE, 9907, 99070K
Maksimov, A. F., Balega, Yu. Yu., Dyachenko, V. V., et al. 2009, AstBull, 64, 296
Mason, B. D., Wycoff, G. L., Hartkopf, W. I., et al. 2001, AJ, 122, 3466 (WDS)
Mason, B. D., Hartkopf, W. I., & Tokovinin, A. 2010, AJ, 140, 735
McAlister, H., Hartkopf, W. I., & Franz, O. G. 1990, AJ, 99, 965
Mendez, R. A., Claveria, R. M., Orchad, M. E., & Silva, J. F. 2017, AJ, 154, 187

Riddle, R. L., Tokovinin, A., Mason, B. D., et al. 2015, ApJ, 799, 4
Schmitt, J. R., Tokovinin, A., Wang, Ji, et al. 2016, AJ, 151, 159
Sebring, T. A., Krabbendam, V. L., & Heathcote, S. 2002, Proc. SPIE, 4837, 71
Tighe, R., Tokovinin, A., Schurter, P., et al. 2016, Proc. SPIE, 9908, 99083B
Tokovinin, A., & Cantarutti, R. 2008, PASP, 120, 170
Tokovinin, A., Mason, B. D., & Hartkopf, W. I. 2010a, AJ, 139, 743
Tokovinin, A., Cantarutti, R., & Tighe, R. 2010b, PASP, 122, 1483
Tokovinin, A., Gorynya, N. A., & Morrell, N. I. 2014, MNRAS, 443, 3082
Tokovinin, A., Latham, D. W., & Mason, B. D. 2015a, AJ, 149, 195
Tokovinin, A., Mason, B. D., Hartkopf, W. I., et al. 2015b, AJ, 150, 50
Tokovinin, A., Mason, B. D., Hartkopf, W. I., et al. 2016a, AJ, 151, 153
Tokovinin, A., Cantaritti, R., Tighe, R., et al. 2016b, PASP, 128, 125003
Tokovinin, A., & Latham, D. W. 2017, ApJ, 838, 54
Tokovinin, A., Mason, B. D., Hartkopf, W. I., et al. 2018, AJ, submitted
Tokovinin, A. 2012, AJ, 144, 56
Tokovinin, A. 2014a, AJ, 147, 86
Tokovinin, A. 2014b, AJ, 148, 72
Tokovinin, A. 2016a, AJ, 152, 10
Tokovinin, A. 2016b, AJ, 152, 11
Tokovinin, A. 2016c, AJ, 152, 138
Tokovinin, A. 2016d, ApJ, 831, 151
Tokovinin, A. 2017, AJ, 154, 110
Velasco, S., Rebolo, R., Oscoz, A., et al. 2016, MNRAS, 460, 3519